The Astrophysical Journal, 980:162 (13pp), 2025 February 20 https://doi.org/10.3847/1538-4357/adad66

ASKAP Observations of the Radio Shell in the Composite Supernova Remnant G310.6-1.6

Wenhui Jing[1], Jennifer L. West[2], Xiaohui Sun[1], Wasim Raja[3], Xianghua Li[1], Lingxiao Dang[4], Ping Zhou[4,5], Miroslav D. Filipović[6], Andrew M. Hopkins[7], Roland Kothes[2], Sanja Lazarević[3,6,8], Denis Leahy[9], Emil Lenc[3], Yik Ki Ma[10,11], and Cameron L. Van Eck[10]

[1] School of Physics and Astronomy, Yunnan University, Kunming, 650091, People's Republic of China; wh.jing@outlook.com, xhsun@ynu.edu.cn, xhli@ynu.edu.cn
[2] Dominion Radio Astrophysical Observatory, Herzberg Astronomy & Astrophysics, National Research Council Canada, P.O. Box 248, Penticton, BC V2A 6J9, Canada; jennifer.west@nrc-cnrc.gc.ca
[3] Australia Telescope National Facility, CSIRO, Space and Astronomy, PO Box 76, Epping, NSW 1710, Australia; Wasim.Raja@csiro.au
[4] School of Astronomy & Space Science, Nanjing University, 163 Xianlin Avenue, Nanjing 210023, People's Republic of China
[5] Key Laboratory of Modern Astronomy and Astrophysics, Nanjing University, Ministry of Education, Nanjing 210023, People's Republic of China
[6] Western Sydney University, Locked Bag 1797, Penrith South DC, NSW 2751, Australia
[7] School of Mathematical and Physical Sciences, 12 Wally's Walk, Macquarie University, NSW 2109, Australia
[8] Astronomical Observatory, Volgina 7, 11060 Belgrade, Serbia
[9] Department of Physics and Astronomy University of Calgary, Calgary, AB, T2N 1N4, Canada
[10] Research School of Astronomy & Astrophysics, The Australian National University, Canberra, ACT 2611, Australia
[11] Max-Planck-Institut für Radioastronomie, Auf dem Hügel 69, 53121 Bonn, Germany
Received 2024 December 6; revised 2025 January 20; accepted 2025 January 21; published 2025 February 12

Abstract

We report the observations of the radio shell of the supernova remnant (SNR) G310.6–1.6 at 943 MHz from the Evolutionary Map of the Universe (EMU) and the Polarization Sky Survey of the Universe's Magnetism (POSSUM) surveys by using the Australian Square Kilometre Array Pathfinder (ASKAP). We detect polarized emission from the central pulsar wind nebula (PWN) with rotation measures varying from –696 rad m^{-2} to –601 rad m^{-2}. We measure the integrated flux density of the shell to be 36.4 ± 2.2 mJy at 943 MHz and derive a spectral index of $\alpha_{\rm pwn} = -0.4 \pm 0.1$ for the PWN and $\alpha_{\rm shell} = -0.7 \pm 0.3$ for the SNR shell. From the combined radio and X-ray observations, the object can be identified as a supernova explosion of about 2500 yr ago with an energy of about 1.3×10^{50} erg, suggesting an ejected mass of about $10\,M_{\odot}$. The circular radio shell outside the circular hard X-ray shell is unique among Galactic SNRs. We discuss several possible scenarios, including blast wave, reverse shock, and pulsar-fed emission, but find that none of them can fully explain the observed characteristics of the shell. This poses a challenge for understanding the evolution of SNRs. The results of this paper demonstrate the potential of the ASKAP EMU and POSSUM surveys to discover more objects of small angular size and low surface brightness.

Unified Astronomy Thesaurus concepts: Interstellar medium (847); Supernova remnants (1667); Radio continuum emission (1340); Magnetic fields (994); Polarimetry (1278); Pulsar wind nebulae (2215)

1. Introduction

Composite supernova remnants (SNRs) consist of a shell and a pulsar wind nebula (PWN) powered by relativistic particles from the associated pulsar (G. Dubner & E. Giacani 2015; J. Vink 2020). According to the catalog compiled by G. Ferrand & S. Safi-Harb (2012), only a handful of them exhibit well-defined circular shells surrounding the PWN in radio or X-ray images. Although spherical symmetry has been suggested as a possible feature of some composite SNRs, there is no evidence to show a correlation between this symmetry and other SNR parameters, such as spectral indices, SNR ages, molecular cloud (MC) associations, or Galactic locations (S. Ranasinghe & D. Leahy 2023). Each of them has shown its individual properties and has provided us with valuable insight into the SNR system.

G310.6–1.6 (R.A. = $14^{\rm h}00^{\rm m}45^{\rm s}$, decl. = $-63°26'$, J2000) is considered to be a composite SNR with a bright central PWN and a circular shell. It was first identified as a PWN from Chandra X-ray observations by J. A. Tomsick et al. (2009). M. Renaud et al. (2010) detected the associated pulsar PSR J1400–6345 from both X-ray and radio timing observations, with a period of 31.18 ms.

The characteristic age is about 12.7 kyr, and the spindown luminosity is about 5.1×10^{37} erg s^{-1} for the pulsar (M. Renaud et al. 2010), making it one of the most energetic Galactic pulsars known. M. Renaud et al. (2010) also discovered the faint shell from the Chandra X-ray image and thus identified G310.6–1.6 as a composite SNR. They examined archival radio observations and obtained a spectral index $\alpha_{\rm pwn} = -0.3$, defined by $S_\nu \propto \nu^{\alpha}$, where S_ν is the flux density at frequency ν. It confirms the identification of the central object as a PWN, which is consistent with expectations (S. P. Reynolds et al. 2012).

S. P. Reynolds & K. J. Borkowski (2019) analyzed the Chandra X-ray observations of a much longer exposure time than that in M. Renaud et al. (2010), and found that the X-ray spectrum of the shell is featureless and can be well fitted with a model of synchrotron radiation. This placed G310.6–1.6 into the category of X-ray synchrotron SNRs (XSSNRs). XSSNRs refer to SNRs with X-ray emission from the shell dominated

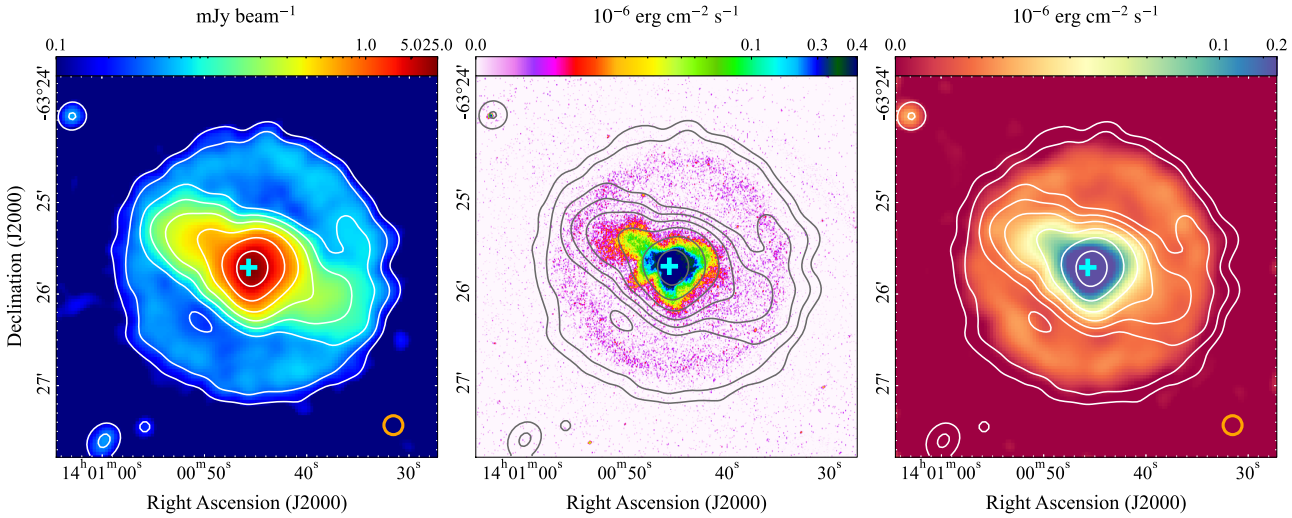

Figure 1. Left: ASKAP MFS Stokes I image at 943 MHz with an angular resolution of 12.″4, shown by the orange circle in the bottom-right-hand corner. Middle: Chandra X-ray photon image averaged across the 1.0–8.0 keV band with an angular resolution of 0.″5. Right: the same as the middle panel, but with the X-ray image smoothed to 12.″4. All contours show the ASKAP Stokes I in the levels of $5\sigma \times 2^i$, $i = 0, \ldots, 5$ with the rms noise σ of 30 μJy beam^{-1}. The cyan cross indicates the position of PSR J1400–6325.

by synchrotron radiation (see S. P. Reynolds et al. 2008, for a review). Among the eight XSSNRs identified so far (S. P. Reynolds & K. J. Borkowski 2024), G310.6–1.6 is the only one that has also been classified as a composite SNR.

Given that the synchrotron X-ray emission is probably from the forward shock, radio emission from the shell is expected. There have been no published radio observations dedicated to G310.6–1.6. It was included in several previous surveys, such as the Molonglo Galactic plane survey at 843 MHz (T. Murphy et al. 2007), the Parkes survey of the southern Galactic plane at 2.4 GHz (A. R. Duncan et al. 1995), and the Parkes-MIT-NRAO survey at 4.85 GHz (J. J. Condon et al. 1993; M. R. Griffith & A. E. Wright 1993). However, limited by resolution and sensitivity, these radio images are dominated by the bright PWN, and the putative shell remains elusive. Based on these observations, an upper limit for the surface brightness of the shell was estimated to be about 2.3×10^{-21} W m^{-2} Hz^{-1} sr^{-1} at 1 GHz (M. Renaud et al. 2010). We note that W. Robbins (2014) reported the detection of the radio shell in the PhD thesis based on observations with the Australian Telescope Compact Array at 5.5 and 9 GHz, but did not perform detailed analysis due to the data quality.

The Australian Square Kilometre Array Pathfinder (ASKAP; A. W. Hotan et al. 2021) with its ongoing continuum survey (the Evolutionary Map of the Universe, EMU; R. P. Norris et al. 2011, 2021; A. M. Hopkins et al. 2025, in preparation) and polarization survey (the POlarization Sky Survey of the Universe's Magnetism, POSSUM; B. M. Gaensler et al. 2010; B. M. Gaensler et al. 2024) delivers images with a high sensitivity of 25–30 μJy beam^{-1} and a high resolution of about 15″, allowing us to detect low surface-brightness emission from small, faint shells. This has been demonstrated by B. D. Ball et al. (2023), M. D. Filipović et al. (2023), and S. Lazarević et al. (2024), who discovered new SNRs from the ASKAP data.

In this paper, we report the observation of the radio synchrotron shell of SNR G310.6–1.6 with ASKAP. Data acquisition and reprocessing are described in Section 2, the results of images and spectra are presented in Section 3,

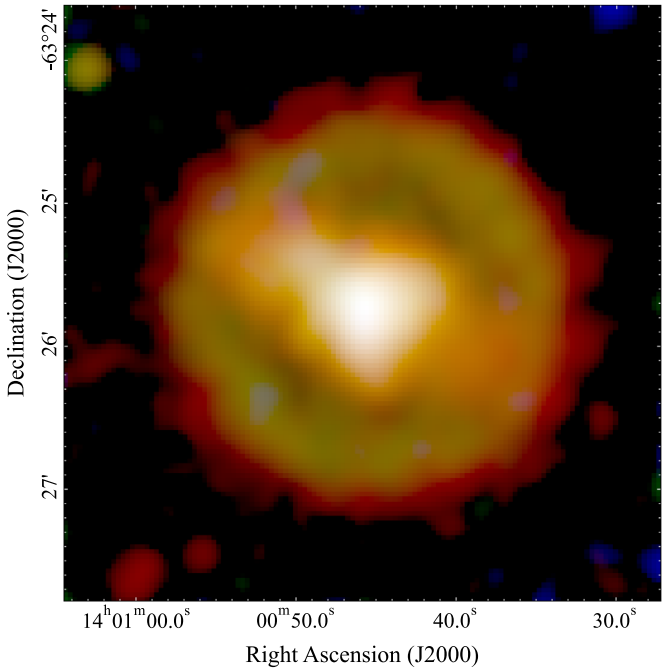

Figure 2. An RGB three-color image with red representing radio emission observed with ASKAP, blue for X-ray emission observed with Chandra in the 0.5–1.2 keV range, and green for X-ray emission in the 1.2–8.0 keV range. All images have a resolution of 12.″4.

discussions of evolution scenarios are given in Section 4, and conclusions are drawn in Section 5.

2. Data Acquisition and Reprocessing

2.1. ASKAP Data

The 30-square degree field containing G310.6–1.6 was observed on 2023 September 30 for 10 hr (ASKAP scheduling block ID 53310) using 36 electronically formed beams arranged in a hexagonal close-pack configuration in the continuum averaged mode where the total frequency bandwidth is divided into 288 1 MHz channels (see Figure 20 in

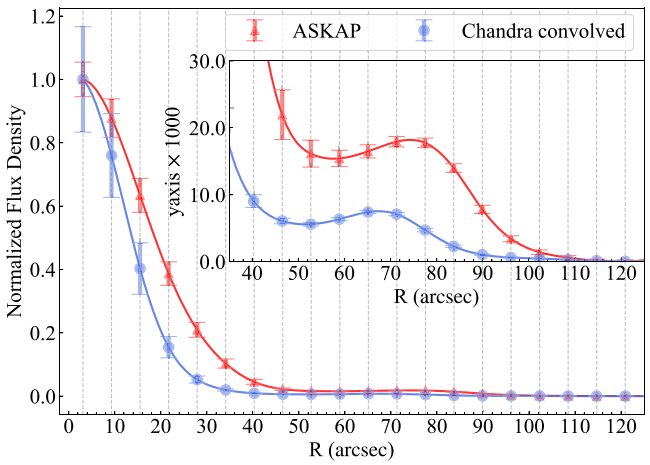

Figure 3. Radial profiles (normalized by their respective maxima) of radio intensity (red) and X-ray photon counts (blue). The inset panel is a zoom-in of the *y*-axis to show the slightly limb-brightened shell. The profiles are derived from the images with a common resolution of 12.″4.

Table 1
Integrated Flux Densities for the Whole SNR, the SNR Shell, and the PWN of G310.6–1.6

Frequency (MHz)	Bandwidth (MHz)	Whole SNR (mJy)	SNR Shell (mJy)	PWN (mJy)
943	288	284.7 (1.2)	36.4 (2.2)	248.3 (1.8)
835	72	298.2 (2.9)	38.5 (2.3)	257.8 (1.7)
908	72	288.7 (2.2)	36.6 (1.7)	250.0 (1.3)
980	72	278.2 (1.7)	34.5 (1.3)	242.2 (0.9)
1051	72	266.3 (1.7)	32.4 (1.1)	232.4 (0.9)

Note. The uncertainties (at the 68% confidence level) are given in parentheses. The region of whole SNR and PWN are defined as the contour levels of 5σ and 20σ shown in Figure 1 (left panel). For the integrated flux density of the SNR shell, the region overlapping with PWN was excluded.

A. W. Hotan et al. 2021). The central frequency of these observations is 943 MHz. The calibrated visibilities for each beam, the mosaicked multifrequency synthesized (MFS) Stokes *I* image, as well as the mosaicked image cubes at 1 MHz resolution for all four Stokes parameters (*I*, *Q*, *U*, and *V*) are available to the public on CSIRO's ASKAP Science Data Archive (CASDA).[12] The images archived on CASDA are convolved to have a matching resolution across all 36 beams. This leads to poorer-than-achievable resolution in parts of the mosaic. The common resolution for the archived MFS images for this observation is 15″, while for the data cubes, the resolution is frequency dependent, with values as coarse as 18″ at the lowest frequencies.

2.2. Images

Full-band MFS Stokes I *image.* We reprocessed the archived calibrated visibilities using ASKAPsoft (J. Guzman et al. 2019). MFS images with the full 288 MHz band for Stokes *I* from beams 27, 28 and 33, containing the SNR in their field of view, are generated, primary-beam corrected, and mosaicked together. The resulting Stokes *I* image has a slightly better resolution of 12.″4 × 12.″4. We used this image for our analyses in the paper.

[12] https://data.csiro.au/collections/domain/casdaObservation/search/

Sub-band MFS Stokes I *images for spectral index measurement.* The MFS imaging algorithm generates images of the Taylor term coefficients. The images of the first two coefficients can be used to compute the spectral indices. But the derived spectral indices using the entire band could be prone to errors, especially for the weak diffused emission from the SNR (for details of these issues, see U. Rau 2010). To compute the in-band spectral indices reliably, we subdivided the visibilities into four spectral windows, each 72 MHz wide, and performed MFS imaging using two Taylor terms producing Stokes *I* images at 835, 908, 980, and 1051 MHz. These images are used in our derivation and analysis of spectral indices.

RM-Synthesis. We convolved the archived Stokes $I(\nu)$, $Q(\nu)$, and $U(\nu)$ spectral data cubes available on CASDA to a common 18″ resolution at all frequencies. We then used the RM-Tools package (C. Purcell et al. 2020) to perform rotation measure (RM) synthesis (M. A. Brentjens & A. G. de Bruyn 2005) and RM clean (G. Heald 2009) to generate the $Q(\phi)$ and $U(\phi)$ data cubes at Faraday depths (ϕ) ranging from -2000 rad m^{-2} to $+2000$ rad m^{-2} in steps of 5 rad m^{-2}. We then searched for peaks in $\sqrt{Q(\phi)^2 + U(\phi)^2}$ along the Faraday depth axis. A detailed description of the procedure can be found in S. Vanderwoude et al. (2024).

2.3. Chandra Data

This SNR has been observed multiple times by the Chandra X-ray observatory since 2006. These observations were carried out with the Advanced CCD Imaging Spectrometer in the Very Faint mode to minimize particle background interference. We used all of the archived data (Chandra ObsID: 9058, 12567, 17905, 19919, 19920, and 21689) to generate the image of photon counts and conduct spectral analysis. Compared to the data set of S. P. Reynolds & K. J. Borkowski (2019), we include two more observations (ObsIDs 9058 and 21689), which contribute an additional exposure time of ∼36 ks.

We analyzed the data with the Chandra Interactive Analysis of Observations software version 4.15 (A. Fruscione et al. 2006). The energy bands in the range of 1.0–8.0 keV were combined to produce the exposure-corrected and energy-filtered image. The total effective exposure time is ∼231.53 ks.

3. Results

The reprocessed ASKAP MFS Stokes *I* image of G310.6–1.6 is shown in Figure 1 (left panel). The frequency is 943 MHz, and the resolution is 12.″4. The rms noise is 30 μJy beam^{-1}. The Chandra X-ray image in the 1.0–8.0 keV bands at the original resolution of 0.″5 and smoothed to the same resolution as the ASKAP image is shown in the middle and right panels, respectively, in Figure 1.

The radio emission of G310.6–1.6 clearly consists of two components: the central PWN and the faint radio SNR shell. The radio PWN running from southwest to northeast is aligned with the X-ray PWN and extends to the edge of the radio emission. Toward the southwest, the brightness falls more rapidly in X-rays than in radio (similar to what is seen in MSH 11-62; P. Slane et al. 2012). Similarly to X-ray, the radio shell is faint and slightly limb-brightened, and has a well-defined circular shape. We derive the flux density and profile of the shell, excluding the portions that overlap with the central PWN.

In Figure 1, we can clearly see that radio emission extends beyond X-ray emission. The mismatch between radio and X-ray

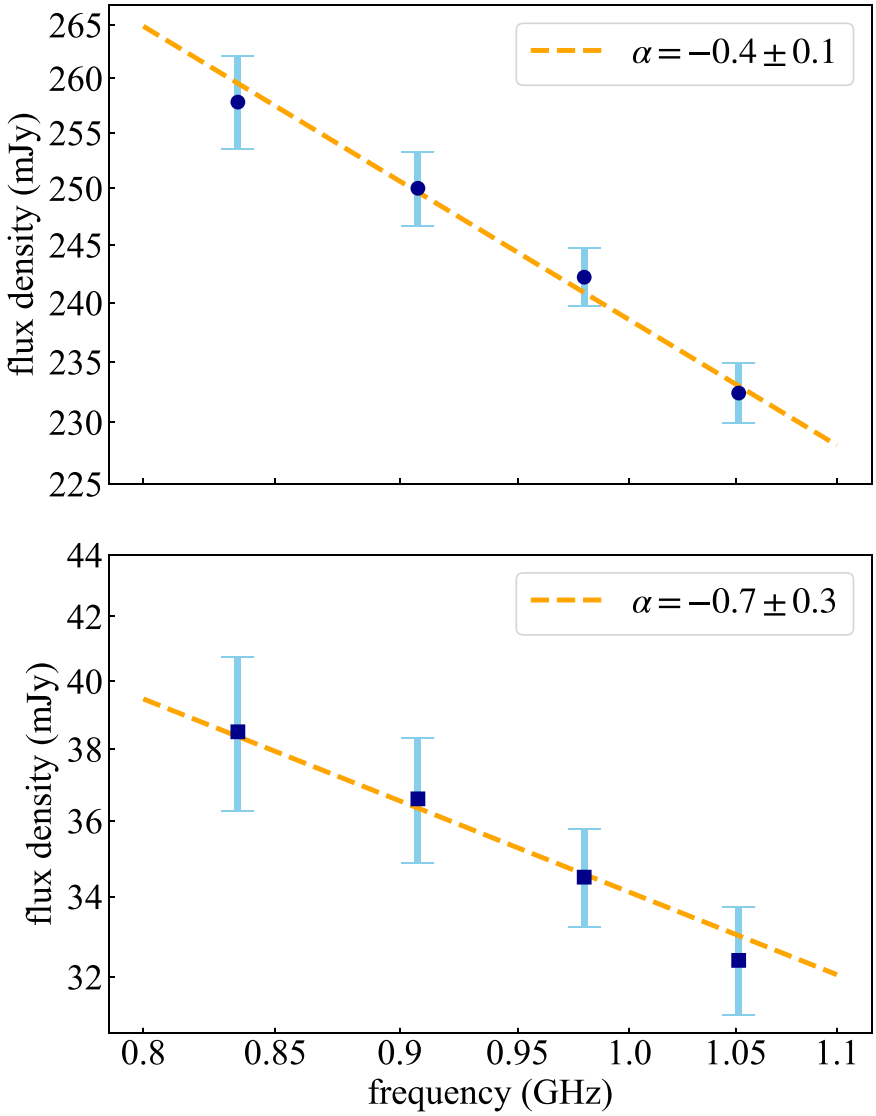

Figure 4. Radio in-band spectra for the PWN (top) and the shell (bottom) of G310.6–1.6 using the flux density values listed in Table 1.

emission from the shell is even more outstanding, as illustrated by the RGB three-color image in Figure 2, which was produced with `multicolorfits` (P. Cigan 2019). Here we split the Chandra band into two ranges: 0.5–1.2 keV (soft) and 1.2–8.0 keV (hard). The radio and X-ray emissions from the central PWN align well overall, but the radio emission is more extended.

Using the same resolution images, we obtain the radial profiles of radio intensity and X-ray photon counts by averaging the values within annuli of 6.″2 width from the geometric center at (R.A. = $14^{h}00^{m}45.^{s}19$, decl. = −63°25′40.″9, J2000) to a radius of 124″. In order to circumvent the influence of the PWN to the SNR shell, we exclude the area with azimuthal angle in the ranges of 18°–100° and 207°–273°, with 0° defined as north and angles measured counterclockwise. Note that both the radio intensity image and the X-ray photon counts image have a resolution of 12.″4, as presented in Figure 1 (left and right panels). To facilitate comparison, the profiles are normalized to a range from 0–1 by their respective maxima, as shown in Figure 3. The zoomed-in panel highlights the slightly limb-brightened shells. The radio shell extends from a radius of about 54″ to a radius of about 100″ with a peak at about 75″. The X-ray shell extends from a radius of about 50″ to a radius of approximately 90″ with a peak at about 66″. The ratio of the width of the shell to the radius of the shell is about 0.45, similar in both radio and X-ray emission. However, the radio shell is shifted outward compared to the X-ray shell, as can be seen from Figures 1 and 2.

We measure the integrated flux densities of the whole SNR, the SNR shell, and the PWN of G310–1.6 from the full-band and the four sub-band MFS Stokes *I* images (Table 1). The integrated flux density of the shell is 36.4 mJy at 943 MHz, corresponding to a surface brightness of about 7×10^{-22} W Hz^{-1} sr^{-1} m^{-2}, well below the upper limit estimated by M. Renaud et al. (2010), explaining its nondetection in previous radio surveys.

3.1. Radio Spectra

The in-band spectra for the central PWN and the shell are derived using the integrated flux densities in Table 1, and are shown in Figure 4.

We obtained a spectral index of $\alpha_{\rm pwn} = -0.4 \pm 0.1$ for the PWN and a spectral index of $\alpha_{\rm shell} = -0.7 \pm 0.3$ for the SNR shell, which fall in the range for PWNe and SNR shells,

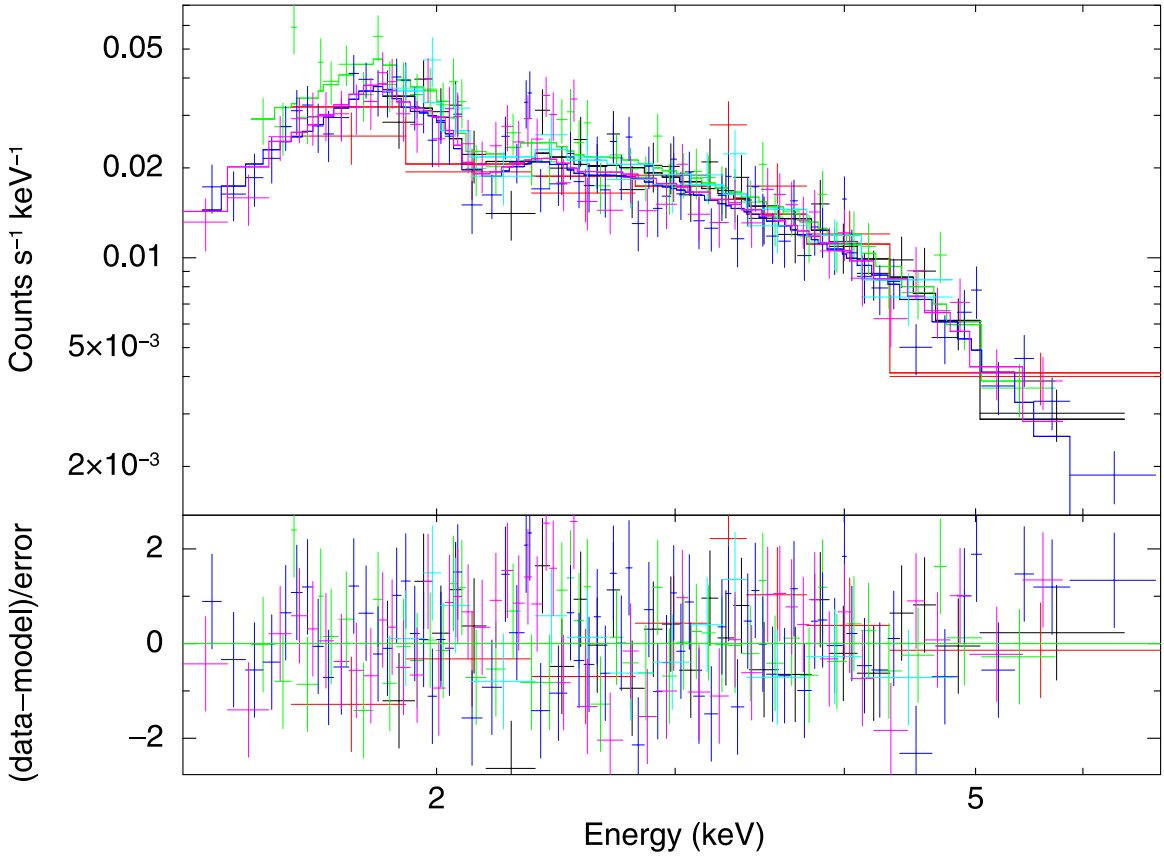

Figure 5. Shell X-ray spectra of G310.6–1.6 fitted with a synchrotron model srcut. The red, green, blue, cyan, magenta, and black colors correspond to the Chandra observation IDs 9058, 12567, 17905, 19919, 19920, and 21689.

Table 2
Results from the Spectral Fits of Shell Using srcut Model

Parameter	Previous Study[a]	This Paper
norm (mJy, input)	$\leqslant 40$	32
$N_{\rm H}$ (10^{22}cm^{-2})	$2.75^{+0.13}_{-0.12}$	$3.34^{+0.21}_{-0.33}$
$\alpha_{\rm shell}$	$-0.49^{+0.1}_{-0.2}$	$-0.46^{+0.03}_{-0.02}$
$\nu_{\rm rolloff}$ (Hz)	$(1.4^{+0.4}_{-0.7}) \times 10^{17}$	$(9.7^{+7.3}_{-2.4}) \times 10^{16}$
χ^2/d.o.f.	...	208.77/215

Note.
[a] The results are from S. P. Reynolds & K. J. Borkowski (2019).

respectively (S. P. Reynolds et al. 2012; R. Kothes 2017). The uncertainties for the spectral indices are derived using the bootstrap method. We created 1000 realizations based on the mean and error for the four data points, and performed linear fittings to obtain 1000 spectral indices. These spectral indices conform to a Gaussian distribution, and its standard deviation was used as the uncertainty shown in Figure 4.

M. Renaud et al. (2010) fit the flux densities measured from previous observations at 843 MHz and 4.85 GHz and obtained a spectral index of $\alpha_{\rm pwn} = -0.33 \pm 0.05$ or $\alpha_{\rm pwn} = -0.205 \pm 0.008$ depending on the methods used to measure the flux density at 4.85 GHz. Their flux densities contain the contribution from the shell, but the contribution is small, only about 12% at frequencies around 943 MHz (Table 1), and expected to be even smaller at higher frequencies with the steep spectrum. Therefore, their spectral index mainly represents the PWN, which is consistent with our result.

3.2. X-Ray Spectra of the Shell

The X-ray spectral analysis by S. P. Reynolds & K. J. Borkowski (2019) uses the upper limit of the radio flux density at 1 GHz for the shell. Since we now have a measurement of the flux density, we use this new measurement in a reanalysis of the X-ray spectral fit.

We retrieve the shell spectra (Figure 5) from six Chandra X-ray observations (ObsIDs: 9058, 12567, 17905, 19919, 19920, and 21689) and rebin them with a minimum signal-to-noise ratio of 5. Different background regions are selected for the observations to ensure that the background spectra and the source spectra are extracted from the same CCD.

Using XSPEC Version 12.14.0 (K. A. Arnaud 1996), we jointly fit the spectra with an absorbed (tbabs) synchrotron (srcut) model with a constant component added to account for calibration uncertainty between observations (<10%). This synchrotron model describes the spectrum of electrons with an exponential cutoff power-law distribution in a homogeneous magnetic field. Note that we select the SNR shell region that clearly emits both radio and X-ray emissions, excluding areas such as the northwest and southeast parts between the PWN and the shell structure. As a result, the selected region is slightly different from that used for deriving the integrated flux density shown in Table 1. We measure the integrated flux density for this region and scale this value to 1 GHz using our measurement of $\alpha_{\rm shell} = -0.7$ to obtain a value of 0.032 ± 0.003 Jy for the model parameter "norm." The solar abundances of M. Asplund et al. (2009) were adopted in the absorption model. As shown in Figure 5, the srcut model can well fit the shell spectra, providing a reduced χ^2/d.o.f. of 0.97.

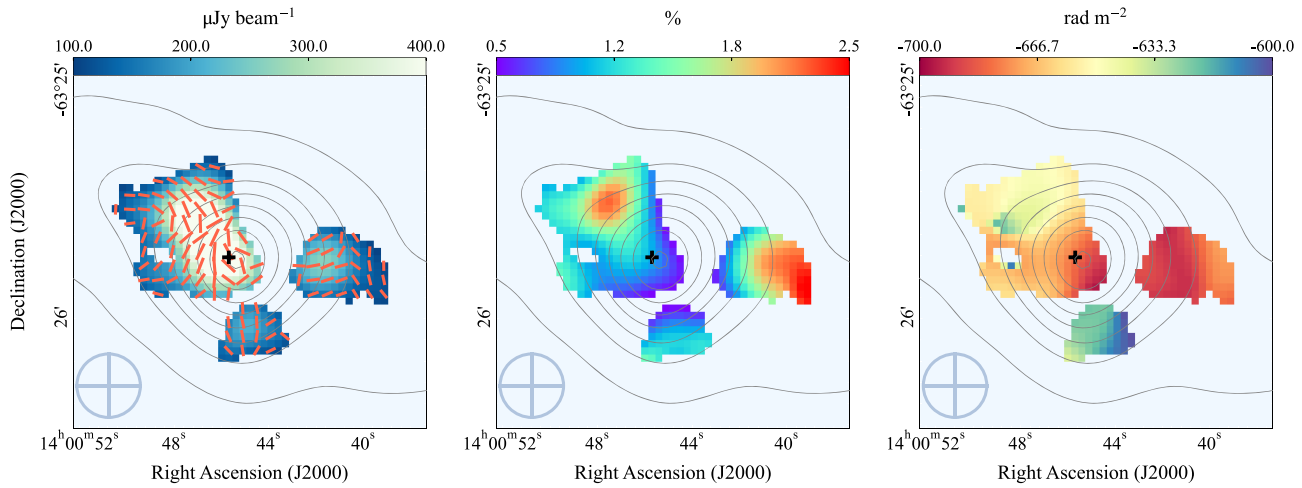

Figure 6. Left panel: polarized intensity image of the PWN overlaid with bars indicating orientation of magnetic field corrected for RM. The length of the bars has been scaled to the square root of the polarized intensity to enhance the visibility of the orientation. Middle panel: fractional polarization image. Right panel: RM image. The position of PSR J1400–6325 is marked with a cross. The contours display the total intensity with levels starting from 2 mJy beam^{-1} and in steps of 6 mJy beam^{-1}. All of the images have a resolution of 18″ shown by the blue ellipse in the bottom-left-hand corner.

The results are shown in Table 2, where $N_{\rm H}$ represents the equivalent hydrogen column density, $\nu_{\rm rolloff}$ indicates the rolloff frequency, and $\alpha_{\rm shell}$ is the fitted radio spectral index. We note that within the uncertainties, this fitted value is in agreement with our measured value. Varying the norm value between 29 and 35 mJy causes a minimal change in the fitting results. This means that the spectral index between X-ray and radio emission is much flatter than measured between radio bands. Fixing $\alpha_{\rm shell} = -0.6$ or -0.7 results in a poor fit to the X-ray spectra.

To assess the contribution of thermal emission, we fit the spectra with a power law plus a plane-parallel shocked plasma model (pshock) following S. P. Reynolds & K. J. Borkowski (2019). Adding this thermal component does not significantly improve the spectral fit according to the F-test[13] (probability = 0.88). The parameters of the pshock model cannot be constrained, and there is a degeneracy between the electron temperature kT_e and the "norm" value of this model ($\propto n_e^2$, with n_e the electron density). We estimate the preshock density $n_0 = n_e/4.8 < 26/0.93/0.16/0.08 f^{-0.5}\,{\rm cm}^{-3}$ for $kT_e = 0.1/0.3/1/3$ keV, where $f \leqslant 1$ is the volume filling factor of the X-ray-emitting gas. The density is different from the one obtained by S. P. Reynolds & K. J. Borkowski (2019). Our study adds two new Chandra spectra and uses the updated solar abundance table (M. Asplund et al. 2009), which can cause some differences in the spectral fit, especially considering that the thermal component is not significantly detected.

3.3. Polarization

The fitted peak polarized intensity (*PI*), the fractional polarization (p, defined as $p = PI/I$), and the fitted peak Faraday depth images derived from RM synthesis[14] are shown in Figure 6. In the case of G310.6–1.6, the strongest peak for a given sight line is the dominant emission component, and the fitted peak Faraday depth is regarded as RM. The orientation of the magnetic field corrected for Faraday rotation is also displayed in Figure 6. S. Vanderwoude et al. (2024) found that the residual off-axis polarization leakage, based on the correction using holographic beam measurements in pilot data, is about 0.5%. The full-survey POSSUM data is expected to achieve residual off-axis leakage as low as 0.2% (Gaensler et al. 2024, submitted). We therefore set a cutoff of 8 for signal-to-noise ratio in *PI* and 0.5% for the fractional polarization. The panels in Figure 6 only show pixels where the values are above these cutoffs.

We detect polarized emission from several segments close to the center of the PWN. The fractional polarization ranges from 0.5% to about 2.5%. The RMs of the polarized segments range from –601 rad m^{-2} to -696 rad m^{-2}, with uncertainties less than about 2 rad m^{-2}. The polarization vectors appear to be coherent in these patches, and the distribution of RMs bears the signature of a toroidal field expected in a PWN (e.g., R. Kothes et al. 2006). We discuss these in Section 4.

For most parts of the remnant, including the shell, the peak polarized intensity image shown in Figure 6 does not show polarized emission above our cutoff values. To look for polarized emission with a higher signal-to-noise ratio, we take advantage of the shell's symmetry and look at radial profiles of linearly polarized quantities: the polarized intensity (*PI*) and the fractional polarization (p). The radial profiles are computed from the *PI* image (Figure 6) and the MFS Stokes *I* image, which is convolved to 18″ to match the resolution of the *PI* image. The centers of the annuli are the same as in Figure 3. The widths of the annuli are set to 9″ and the radius of the largest annulus is set to 180″. The resulted radial profiles are shown in Figure 7.

For the radial profiles of total intensity and polarized intensity, we plot the mean of the points within corresponding annuli in the respective images. The error bars show the corresponding standard deviations of the quantities. For fractional polarization, the radial profile shows the ratio of the *PI* profile to that of the Stokes *I* profile. The error bars show the standard deviations (within the respective annuli) in the fractional polarization derived as the ratio of the *PI* noise image (measured in a signal-free frame with the Faraday depth of 2000 rad m^{-2}) and the Stokes *I* image.

As can be seen from the radial profile of fractional polarization (see Figure 7), there is significant polarized

[13] https://heasarc.gsfc.nasa.gov/xanadu/xspec/manual/node82.html
[14] Using the rmtools_peakfitcube tool from RM-Tools.

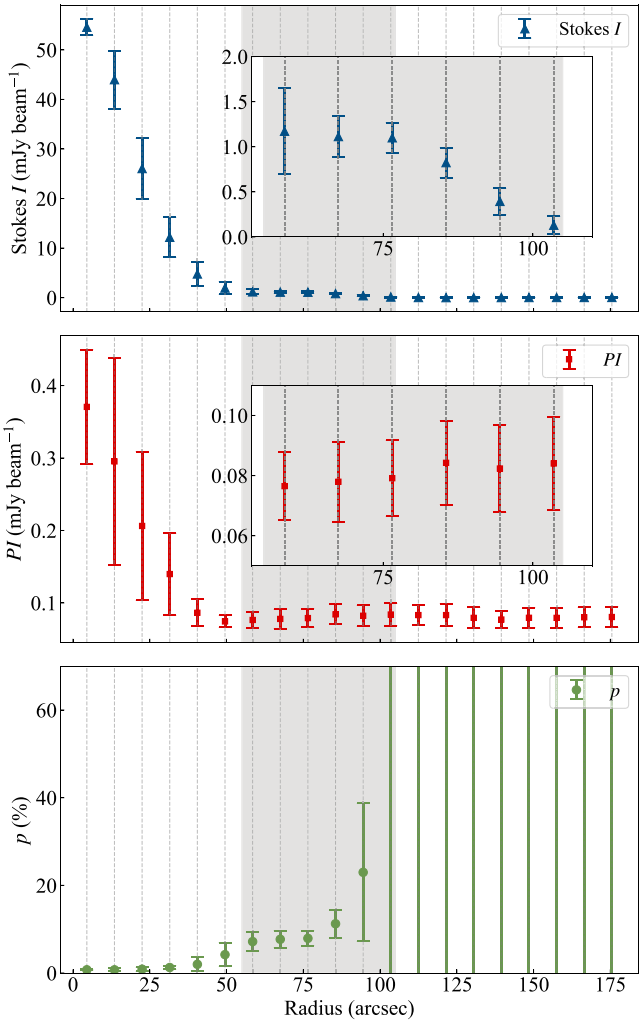

Figure 7. Radial profiles of radio total intensity (Stokes *I*, blue, top panel), polarization intensity (*PI*, red, center panel), and fractional polarization (*p*, green, bottom panel). The inset panel shows the profile across the full radial extent, while the right panel zooms in on *y*-axis to show the faint structure. The gray region indicates where the shell is located.

emission, particularly in the limb-brightened parts of the SNR shell. This provides additional independent evidence of the emission from the shell being synchrotron in nature. We discuss the details in Section 4.

4. Discussions

M. Renaud et al. (2010) combined the dispersion measure (DM) of the pulsar PSR J1400–6325, the extinction from the H I column density obtained from X-ray spectral fitting, and the relation between spindown power and X-ray luminosity to derive a distance of 7 kpc for G310.6–1.6, which puts the SNR at the Crux-Scutum spiral arm. We adopt this distance for the discussions hereafter.

4.1. Radio Spectro-polarimetry

SNR shells are expected to emit synchrotron emission. While the derived spectral index $\alpha_{\rm shell} = -0.7 \pm 0.3$, discussed in Section 3.1, is consistent with synchrotron emission, linearly polarized emission provides a more direct evidence. Detections of polarization are challenging, especially when the emission is weakly polarized, as is the case here.

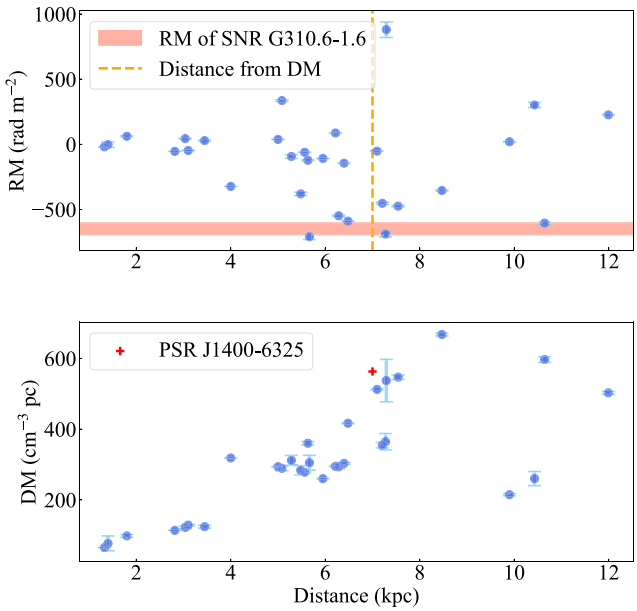

Figure 8. RM (top) and DM (bottom) vs. distance for pulsars within 5° of PSR J1400–6325, which is marked by a cross. The RM value of G310.6–1.6 is from –696 rad m^{-2} to –601 rad m^{-2}. The dashed line indicates the distance of 7 kpc.

From the radial polarization profiles shown in Figure 7, we find evidence of polarization from the remnant, with $p \sim 5\%$ in the shell region and reaching upwards of 10% near the outer edges of the shell ($\sim 100''$), beyond which the fractional polarization is dominated by noise. For the central regions of the remnant, the fractional polarization is very low.

For the whole SNR, the fractional polarization we detect is much less than the theoretical value of $p \sim 70\%$ expected from synchrotron emission (e.g., A. G. Pacholczyk 1970). The difference between what we observe and this theoretical value can be due to the Stokes *I* emission having contributions from mechanisms other than synchrotron emission. Low polarized fractions can also be due to depolarization from destructive interference of the polarization vectors either along the line of sight (field reversals and/or mixing of Faraday-rotating thermal and synchrotron-emitting nonthermal plasma) or within the beam of the telescope. At low frequencies, this depolarization can be enhanced by Faraday rotation effects. At high frequencies, where Faraday rotation is negligible, depolarization is purely due to geometry of the intrinsic magnetic field.

High-frequency (10 GHz) observations of PWNe have detected $p = 10\%$ for CTB 87 (R. Kothes et al. 2020), and $p = 24\%$ for DA 495 (R. Kothes et al. 2008). In the case of G310.6–1.6, if we assume a similar intrinsic value of $p \sim 20\%$, then our observed polarized fraction of $p \sim 1\%$ at 943 MHz indicates a significant depolarization factor of $\sim$0.05. Ascertaining these will require future observations of G310.6–1.6 at suitable frequencies and bandwidth.

4.2. RM

The RMs of the polarization segments, shown in Figure 6, include contributions from both the magneto-ionic medium of the PWN itself and also a foreground component that comes from the interstellar medium of the Milky Way along the line of sight. In order to analyze the contribution from the PWN, we must first estimate and remove the foreground. We use two methods to estimate the foreground: the first is based on nearby

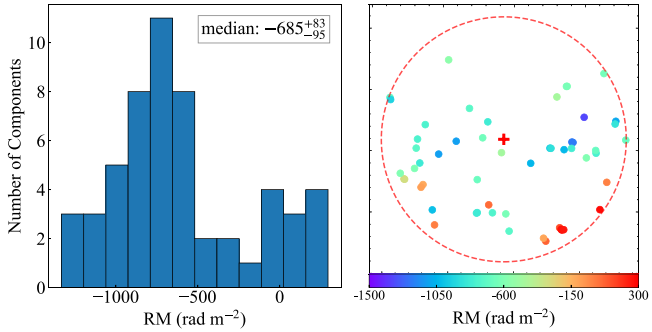

Figure 9. Histogram of RM values of polarized components within 1° of the PWN (left) and RM spatial distribution in the J2000 coordinate system (right). The red dashed line circle indicates a radius of 1°, and the red cross indicates the location of SNR G310.6–1.6.

pulsars, and the other is based on the RM distribution of polarized components detected in the POSSUM survey. We use the term "components" instead of "sources," as a single background synchrotron source can consist of multiple components, each with its own RM (see S. Vanderwoude et al. 2024, for a detailed explanation).

We retrieve pulsars within 5° of PSR J1400–6325 from the ATNF pulsar catalog[15] (R. N. Manchester et al. 2005), plotting RM and DM against distance[16] in Figure 8. There is a linear relationship between DM and distance until a distance of about 8 kpc, while the RMs have a large scatter. The median RM for pulsars between 6 kpc and 8 kpc is about –450 rad m^{-2}. The three pulsars with angular separations <2° have RMs of –474 rad m^{-2}, –589 rad m^{-2}, and –709 rad m^{-2}, leading to an average value of –590 rad m^{-2} with a scatter of about 120 rad m^{-2}.

We analyze polarized components located within 1° of G310.6–1.6. For this analysis, we used the preliminary catalog of polarized components that is available on CASDA. For components that are $<0.^{\circ}01$ apart, we treated them as one component and used their average RM values. A total of 54 components were selected, and their RM distributions are shown in the histogram (Figure 9) along with their locations in the sky. The histogram on the left of Figure 9 indicates that the RM values vary widely, reflecting contributions from both within the polarized components and variations in the foreground RM. To estimate the foreground RM contribution, we calculated the median RM value using bootstrap resampling, obtaining a value of -685^{+83}_{-95} rad m^{-2}, which agrees with the range of the pulsar RMs. This value, derived from more lines of sight closer to the SNR than pulsars, is adopted as the foreground RM for the following analysis. In Figure 10 we show the resulting RM after subtracting the average foreground RM of -685 rad m^{-2}.

4.2.1. RM Variation

The observed RM of the PWN varies between –696 rad m^{-2} and –601 rad m^{-2}, and the RM variation is up to about 100 rad m^{-2}. This variation could result from either Galactic RM fluctuations or internal RM within the PWN itself.

To estimate the Galactic RM variation, we use the RM structure function ($D_{\rm RM}$) from M. Haverkorn et al. (2008). From their Figure 1, the structure function for the Crux arm,

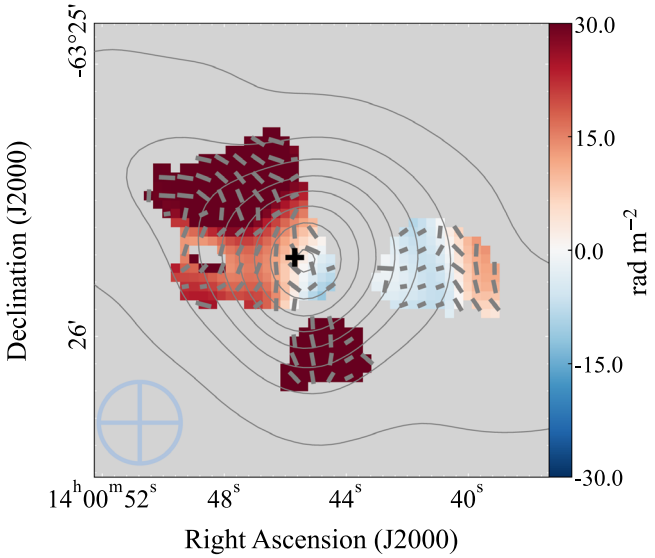

Figure 10. RM variation for the central area of PWN after subtracting the foreground RM contribution of -685 rad m^{-2} from the RM map shown in Figure 6 (right panel). The length of the gray bars has been scaled to the square root of the polarized intensity to enhance the visibility of the orientation.

where G310.6–1.6 is located, is flat regarding with the angular separation. In this case, $D_{\rm RM} = 2\sigma^2_{\rm RM}$, and the RM scattering $\sigma_{\rm RM}$ is about 130 rad m^{-2}. This can explain the observed RM variation. However, such a large foreground RM variation would produce a totally distorted polarization angle distribution, which is not the case shown in Figure 6.

It is more likely that the variation in RM is indicative of internal RMs, meaning that there are thermal electrons inside the PWN. With a foreground RM of –685 rad m^{-2}, the internal RM is in the range of approximately from –85 rad m^{-2} to +10 rad m^{-2}, as shown in Figure 10. The values of internal RMs depend on the foreground RM, which is very uncertain. To produce the observed maximum internal RM difference of about 100 rad m^{-2}, the absolute values of internal RM for parts of the PWN are required to be greater than half of the difference, namely about 50 rad m^{-2}.

If we assume that relativistic and thermal electrons are uniformly mixed, then the differential Faraday rotation along the line of sight will cause depolarization, and the depolarization factor can be calculated as $|\sin(2\Delta{\rm RM}\lambda^2)/(2\Delta{\rm RM}\lambda^2)|$, where ΔRM is the internal RM (D. D. Sokoloff et al. 1998). The depolarization factor of 0.05 from Section 4.1 thus leads to an observed absolute value of the internal RM of 100 rad m^{-2} or less. Larger absolute values of internal RMs will result in almost total depolarization.

In summary, we conclude that the bulk of the RM contribution comes from the Milky Way foreground. However, the evidence presented here supports the existence of internal RM from the PWN. We used an absolute value of 50 rad m^{-2} for the internal RM when estimating the lower limit of the thermal electron density inside the PWN in the analysis below.

4.3. Magnetic Field

The RM image in Figure 10 exhibits a positive sign in the northeastern patch and a negative sign in the central and western regions. Note that the positive sign indicates a magnetic field pointing toward us and vice versa for the negative sign. This suggests the existence of a toroidal field, which is very common for PWNe (R. Kothes et al. 2006). The

[15] https://www.atnf.csiro.au/research/pulsar/psrcat/

[16] The best estimate of the pulsar distance using the YMW16 (J. M. Yao et al. 2017) DM-based distance as default (kiloparsecs).

polarization angles across these areas remain relatively uniform, implying that the toroidal field is shaping both the RM and the observed polarization features. However, there are further sign changes toward the west, which challenges the interpretation. It could be that there exists an extra poloidal field component (S. P. Reynolds et al. 2012), which disrupts the coherent magnetic field. Higher-frequency and higher-resolution observations are needed to further investigate these RM patterns and clarify the underlying structures.

The magnetic field strength can be estimated by assuming the energy equipartition (A. G. Pacholczyk 1970) between cosmic-ray particles and the magnetic field as

$$B = 4.5^{2/7}(1+k)^{2/7}c_{12}^{2/7}f^{-2/7}R^{-6/7}L^{2/7}. \quad (1)$$

where k is the ratio of proton energy to electron energy, f is the volume filling factor, R is the radius, L is the radio luminosity, and c_{12} is a constant. We used $k = 100$ estimated by R. Beck & M. Krause (2005), and the frequency range of 10^7–10^{10} Hz for the integral of luminosity. In this way, the equipartition magnetic field was estimated to be about 120 μG for the PWN of G310.6–1.6. We note that the equipartition condition might not hold for PWNe, but it is still worthwhile to compare the equipartition value with those estimated from other methods, as has been done for PWN G327.1–1.1 (Y. K. Ma et al. 2016).

There are no stringent constraints of the magnetic field from high-energy observations of the PWN. The nondetection of teraelectronvolt photons put a lower limit of about 6 μG for the magnetic field (M. Renaud et al. 2010). There is a break at about 6 keV (M. Renaud et al. 2010) or 4.2 keV (A. Bamba et al. 2022) from X-ray observations. If the break was caused by synchrotron cooling, the magnetic field would be small, about 10 μG; otherwise, G310.6–1.6 would be too young (M. Renaud et al. 2010). However, the break can be interpreted as the cutoff at high energies for injected electrons (e.g., J. Martin et al. 2014; see their Figure 4). Interestingly, a model with a magnetic field of up to about 300 μG can still fit the broad spectrum from radio to teraelectronvolts (J. Martin et al. 2014).

There is a spectral break at the frequency of about 10^{14} Hz between radio with $\alpha_{\rm pwn} = -0.4$ and X-ray with $\alpha_{\rm pwn} = -1$ from a photon spectral index of about 2 (A. Bamba et al. 2022). The break has been well reproduced with a broken power law for the injected electrons (S. J. Tanaka & F. Takahara 2013; J. Martin et al. 2014; B.-T. Zhu et al. 2018). However, the radio emission extending beyond the X-ray emission (Figure 2) also favors the scenario of synchrotron cooling. The magnetic field B in μG and the age t_3 in 10^3 yr can be related as $B = 215t_3^{-2/3}$ (B. M. Gaensler & P. O. Slane 2006). For an age of 2500 yr, the magnetic field would be about 120 μG, consistent with the estimate from energy equipartition.

4.4. Preshock Density

To produce the internal RM of 50 rad m^{-2} contributed by the PWN, the minimum electron density is required to be about 0.2 cm^{-3}, assuming that the magnetic field of 120 μG is completely parallel to the line of sight, and the path length is approximately the radio extent of the PWN from the southeast to the northwest with a radius of about 40″ (Figure 3). The actual electron density has to be much larger because a large fraction of the magnetic field is expected to be perpendicular to the line of sight to generate the observed synchrotron emission. With a much smaller magnetic field of about 10 μG (e.g., M. Renaud et al. 2010), the electron density would be even higher. Furthermore, The PWN evolves within the ejected mass of the progenitor star, where the region with the highest electron density is still at the forward shock of the SNR (J. M. Blondin et al. 2001). The electron density of the shell (preshock density) is not expected to be lower than the electron density derived from the PWN.

The radio luminosity of the SNR shell is about 2×10^{21} erg s^{-1} Hz^{-1} at 1 GHz with a spectral index of $\alpha_{\rm shell} = -0.7 \pm 0.3$. To produce such a low luminosity, either the supernova explosion energy, $E_{\rm sn}$, or the preshock density n_0 must be low. According to E. G. Berezhko & H. J. Völk (2004; see their Figure 4), to derive the observed luminosity for the SNR shell with a diameter of $2R_{\rm snr} \approx 6.8$ pc, $E_{\rm sn}$ is around 1.6×10^{48} erg with $n_0 = 1$ cm^{-3}, and $E_{\rm sn}$ is around 5×10^{49} erg with $n_0 = 0.1$ cm^{-3}. Note that the simulations by E. G. Berezhko & H. J. Völk (2004) used an ejected mass $M_{\rm ej} = 1.4M_\odot$. If the ejected mass is increased to a typical value of $10M_\odot$, the explosion energy is correspondingly increased to about 1.3×10^{50} erg to produce the same radio luminosity, according to E. G. Berezhko & H. J. Völk (2004).

We take $E_{\rm sn} = 1.3 \times 10^{50}$ erg, $n_0 = 0.1$ cm^{-3}, and $M_{\rm ej} = 10M_\odot$ for the analysis below. These values are also consistent with the correlation between $E_{\rm sn}$ and $M_{\rm ej}$ derived by O. Pejcha & J. L. Prieto (2015). We note that the preshock density used in this study is larger than the value of 0.01 cm^{-3} given by S. P. Reynolds & K. J. Borkowski (2019) using X-ray analysis, but consistent with our updated X-ray analysis (see Section 3.2).

4.5. Age

Suppose a spherical explosion with a density of $n_0 = 0.1$ cm^{-3}: the mass swept up by the SNR shell is about $0.6M_\odot$, which is much smaller than the ejected mass. This means that the SNR shell is likely still in the free expansion phase. The expansion speed can be estimated as $\sqrt{2E_{\rm sn}/M_{\rm ej}}$, which is about 1200 km s^{-1}, implying an age of about 2770 yr. This roughly agrees with the age of 2500 yr estimated from synchrotron cooling.

The ratio of the PWN radius to the radius of the SNR shell ($\mathcal{R}$) indicates the evolution of the object (e.g., E. van der Swaluw & Y. Wu 2001). $\mathcal{R}$ can be better determined from the radio image than from the X-ray image because the lifetime of the radio-emitting electrons is much longer than that of the X-ray-emitting electrons. As can be seen in Figure 2, $\mathcal{R}$ is about 0.4 from the southeast to the northwest and is close to 0.9 from the southwest to the northeast.

According to E. van der Swaluw & Y. Wu (2001), the ratio can be represented as $\mathcal{R}(t) \approx \eta_3(t)(E_{\rm sd}/E_{\rm sn})^{1/3}$, where $\eta_3(t)$ was introduced as an additional dimensionless parameter and is between 1 and 3 for the first several thousand years and almost constant close to 1 afterward. $E_{\rm sd}$ is the spindown energy driving the PWN. For an age $t = 2500$ yr, $E_{\rm sd} \approx \dot{E}t$ is about 4.02×10^{48} erg, where $\dot{E}$ is the spindown luminosity of the pulsar. These values lead to $\mathcal{R}(t) \approx 0.3\eta_3(t)$. With an η_3 of about 3, the observed $\mathcal{R}$ from the radio image can be explained.

The radius of the PWN can be estimated with $\dot{E}$, $E_{\rm sn}$, $M_{\rm ej}$, and t (B. M. Gaensler & P. O. Slane 2006), which is about 1.6 pc with $t = 2500$ yr. This is consistent with the PWN radius of about 40″ or 1.4 pc from the southeast to the northwest.

In addition, the steep radio spectral index of $\alpha_{\rm shell} = -0.7 \pm 0.3$ is typical for a young SNR still in the free expansion phase (S. Ranasinghe & D. Leahy 2023). From the X-ray expansion study, a lower limit of 2500 yr for the age was derived by S. P. Reynolds & K. J. Borkowski (2019). These corroborate our estimate, and we use the age of 2500 yr for the analysis below.

4.6. Origin of the SNR Shell

S. P. Reynolds & K. J. Borkowski (2019) presented several scenarios to interpret the SNR shell, such as the blast wave, reverse shock, pulsar-fed emission, and low-energy supernovae, but none are conclusive. Based on our analyses above, we proposed an $E_{\rm sn}$ of 1.3×10^{50} erg, much larger than the upper limit $E_{\rm sn}$ of 3×10^{47} erg by S. P. Reynolds & K. J. Borkowski (2019). We thus only discuss the first three scenarios below.

4.6.1. Blast Wave

In this scenario, both the X-ray and radio emissions are from the forward shock. The X-ray emission is from the teraelectronvolt electrons, and thus traces the front of the forward shock where the acceleration efficiency is high. Because of synchrotron cooling, only the recently accelerated electrons produce the observed X-rays. In contrast, radio emission is from lower-energy electrons and cooling can usually be neglected. Therefore, it is expected that the X-ray emission is outside of the radio emission, as has been shown by theoretical calculations and simulations (S. P. Reynolds & R. A. Chevalier 1981; G. Cassam-Chenaï et al. 2005). This has also been observed for SNRs with synchrotron X-ray emission, such as SNR G347.3–0.5 (J. S. Lazendic et al. 2004; see their Figure 9) and SNR G32.4+0.1 (S. P. Reynolds & K. J. Borkowski 2024; see their Figure 4). However, this contradicts the observations shown in Figures 2 and 3, where the radio emission is clearly outside the X-ray emission. Therefore, the blast wave scenario is not favored.

Another assumption is that the mismatch between the X-ray and radio emission from the forward shock are caused by expansion. If we consider the mismatch of the shell starting from 2016 and evolving to 2023, the expansion speed would reach $1\farcs28\ {\rm yr}^{-1}$, or approximately 40,000 km s^{-1} at a distance of 7 kpc, corresponding to an expansion rate of 1.9% yr^{-1}. The results conflict with the upper limit of the shock expansion velocity of just 1000 km s^{-1} given by S. P. Reynolds & K. J. Borkowski (2019). Longer-term observations in the future, especially high-resolution X-ray observations, will help address this issue by analyzing the expansion velocity of the blast wave.

4.6.2. Reverse Shock

The inward-facing reverse shock can also accelerate particles based on the theoretical modeling of D. C. Ellison et al. (2005). Observational evidence of electrons accelerated to teraelectronvolts by reverse shock has been found for SNRs Cas A (T. Sato et al. 2018) and RCW 86 (J. Rho et al. 2002). The upstream magnetic field for the reverse shock is much weaker than the ambient magnetic field facing the forward shock. Unlike forward shocks, only some reverse shocks can amplify this weak magnetic field to the extent required for high acceleration efficiency. Therefore, it is expected that the majority of the hard X-ray emission is from forward shock, and only a small fraction is from reverse shock, as seen from both Cas A and RCW 86 and from simulations (V. N. Zirakashvili & F. A. Aharonian 2010).

The inward motion of the reverse shock begins at (J. M. Blondin et al. 2001):

$$t \approx 120 (M_{\rm ej}/M_{\odot})^{5/6} n_0^{-1/3} (E_{\rm sn}/10^{51}\,{\rm erg})^{-1/2}\,{\rm yr}. \quad (2)$$

It leads to about 4800 yr for G310.6–1.6. This implies that the acceleration by the reverse shock has not yet begun. Even if reverse shock acceleration occurred, it is puzzling that the whole X-ray shell is inside the radio shell (Figure 2), totally different from Cas A and RCW 86. Therefore, it is certainly imaginable for the X-ray shell to be produced by reverse shock, but challenges remain to make it work practically.

4.6.3. Pulsar-fed Emission

The shape of the PWN depends mainly on the interaction between the pulsar kick velocity, the external density gradient, and magnetic field (J. M. Blondin et al. 2001; E. van der Swaluw 2003; E. van der Swaluw et al. 2004). The simulations by C. Kolb et al. (2017) showed that an external gradient could produce an asymmetric PWN and a circular shell with a pulsar in the center, as in the case of G310.6–1.6.

In the pulsar-fed emission scenario, the high-energy electrons producing the radio and X-ray emission of the SNR shell are both from the pulsar, and the radio peak is expected to be outside the X-ray peak taking into account the cooling. To reach the radio peak at about 75″ (Figure 3) with an age of about 2500 yr, the diffusion coefficient is about 3.9×10^{26} cm^2 s^{-1}, reasonable for particles transporting in PWN (e.g., X. Tang & R. A. Chevalier 2012). The diffusion coefficient is usually energy independent (O. Porth et al. 2016). Therefore, to reach the X-ray peak at about 66″ (Figure 3), the cooling age of the electrons responsible for the X-ray emission should be around 1900 yr. The cooling age can be represented with magnetic field B (in μG) and the energy of the emitting photons $E_{\rm ph}$ (in kiloelectronvolts) as $55.2\ (B/100)^{-3/2} E_{\rm ph}^{-1/2}$ yr (B. Olmi & N. Bucciantini 2023). For $E_{\rm ph} = 2$ keV, the magnetic field is about 7.5 μG, which is also reasonable.

For the pulsar-fed emission scenario to work, it would require the supernovae to explode inside a spherical cavity. Neutral hydrogen (H I) observations are typically used to detect cavities. However, the small angular size of G310.6–1.6 requires sufficiently high-resolution H I data for detection, which are unfortunately not available yet. We still examined low-resolution data sets from the H I 4π survey (HI4PI Collaboration et al. 2016) survey but could not find any cavities associated with G310.6–1.6.

We have also searched infrared data for possible evidence of cavities, such as the Wide-field Infrared Survey Explorer (E. L. Wright et al. 2010) data at 22 μm and 12 μm bands, and the AKARI far-infrared all-sky survey (Y. Doi et al. 2015) at 60 μm, 90 μm, 140 μm, and 160 μm bands. There is no evidence of the cavity that can be identified.

From the radio morphology, the PWN appears to connect with the shell in the northeast and southwest, which leads to an intriguing possibility: High-energy electrons could be tunneled into the shell from the central bar (Figure 2).

Radio observations at higher frequencies are required to establish a spectral index map of G310.6–1.6 to investigate the connection between the PWN and the SNR shell, which is planned and will be presented in a future paper.

4.7. Comparison with Other SNRs

Among Galactic SNRs, G310.6–1.6 is unique and has one of the lowest surface brightnesses. It displays two outstanding characteristics: (i) a central PWN with a circular shell putting it in the group of symmetrical composite SNR, and (ii) a nonthermal X-ray shell putting it into the group of XSSNR. In the context of each group, it possesses an exclusive nature.

4.7.1. Symmetrical Composite SNR

Noticeable SNRs in this group are G11.2–0.3, G292.0+1.8, and G21.5–0.9, which have been discovered to manifest shell structure in X-rays. G11.2–0.3 is one of the youngest core-collapse SNRs in the Milky Way with an age of 1400–2400 yr (K. J. Borkowski et al. 2016). The radio emission from the SNR shell is brighter than that from the PWN, opposite to G310.6–1.6. There is also hard X-ray emission in 5–8 keV from the shell, but its spectrum can be well fit with a combination of vpshock and srcut modes in XSPEC, and the thermal emission is dominant.

G292.0+1.8 is also a core-collapse SNR with an age of around 2500 yr (B. M. Gaensler & B. J. Wallace 2003). It is an oxygen-rich SNR, as can be seen from X-ray observations. The ratio of the radius of the PWN to the radius of the SNR is also large in both radio and X-ray, similar to G310.6–1.6. The SNR is surrounded by a soft X-ray shell (J. Bhalerao et al. 2019).

G21.5–0.9 is also a young SNR with an age in the range 200–1000 yr (F. Bocchino et al. 2005). Similarly to G310.6–1.6, G21.5–0.9 has a limb-brightened X-ray shell that is nonthermal (F. Bocchino et al. 2005; B. T. Guest et al. 2019). However, no radio shell has been detected so far (M. F. Bietenholz & N. Bartel 2008; M. F. Bietenholz et al. 2011).

Recently, another young SNR, G329.9–0.5, has been discovered (Z. J. Smeaton et al. 2024). Although it has a similar morphology as G310.6–1.6 in radio, the correlation between X-ray and radio is still inconclusive.

4.7.2. XSSNR

XSSNRs are the best candidates for studying particle acceleration mechanisms in SNRs. However, as of now, only eight such remnants have been identified in our Galaxy including G310.6–1.6 (S. P. Reynolds & K. J. Borkowski 2024). Given the limited number of samples, each new discovery of XSSNR could provide crucial insights. Except for G310.6–1.6, all other XSSNRs are shell-type SNRs. Some of them may also be associated with a PWN, but such associations await confirmation.

SNRs in this group, such as G1.9+0.3 and SN 1006 have well-defined radio and X-ray shells. Their X-ray shells are bilateral in shape, and the hard X-ray shell is outside the radio shell (G. Cassam-Chenaï et al. 2008; S. P. Reynolds et al. 2008). In contrast, G310.6–1.6 has complete circular radio and X-ray shells, and the radio shell is outside the X-ray shell. For G1.9+0.3, the X-ray shell is brightest toward the east and west, whereas the radio shell is brightest toward the north. The mismatch has been attributed to the interaction with a molecular cloud (R. Enokiya et al. 2023) or the asymmetric circumstellar medium (M. A. Villagran et al. 2024). For SN 1006, the radio and X-ray shells with enhancement in the northeast and southwest limbs are most likely due to a polar cap geometry (S. Katsuda 2017).

5. Conclusions

We presented images of total intensity and polarized intensity of G310.6–1.6 at 943 MHz from the ASKAP EMU and POSSUM surveys.

The weak radio shell with a surface brightness of about 7×10^{-22} W Hz^{-1} sr^{-1} m^{-2} was detected here at 943 MHz. The in-band radio spectral index is -0.7 ± 0.3.

We observed strong radio emission from the central PWN, and obtained an in-band spectral index of -0.4 ± 0.1. Compared with X-ray observations, a spectral break at a frequency of about 10^{14} Hz is expected, which is probably caused by synchrotron cooling. The energy equipartition magnetic field was estimated to be about 120 μG. We also detected polarized emission and obtained an RM between –696 rad m^{-2} and –601 rad m^{-2}. We have also estimated RM contribution from the Milky Way as -685^{+83}_{-95} rad m^{-2}. The variation of RM and depolarization imply internal RM with a typical value of about 50 rad m^{-2}. The variation in the sign of the RM suggests a possible toroidal field.

We suggested an age of about 2500 yr, a supernova explosion energy of 1.3×10^{50} erg, an ejected mass of 10 $M_\odot$, and a preshock density of 0.1 cm^{-3} for G310.6–1.6. Subsequently, the low radio luminosity of the shell, the spectral break at 10^{14} Hz for the PWN, the internal RM of the PWN, and the large ratio between the PWN radius and the SNR radius in radio can be explained.

The radio circular shell outside the hard X-ray circular shell is very unique among SNRs and yet to be understood. Possible scenarios include blast wave, reverse shock, and pulsar-fed emission. However, none of them are able to explain the offsets between the two shells. Further exploration through radio and high-energy observations will be crucial to fully elucidate the origin and evolutionary state of SNR G310.6–1.6.

Our results demonstrate the potential for discovering new objects of small angular size and low surface brightness for the ongoing ASKAP EMU and POSSUM surveys.

Acknowledgments

This research has been supported by the National SKA Program of China (2022SKA0120101). P.Z thanks the support from NSFC grant No.12273010. M.D.F. and S.L. acknowledge Australian Research Council (ARC) funding through grant DP200100784. W.-H. Jing is supported by the Scientific Research Fund Project of Yunnan Education Department (Project ID: 2025Y0015) and Scientific Research and Innovation Project of Postgraduate Students in the Academic Degree of Yunnan University (Project ID: KC-24248558). We thank Dr. Wolfgang Reich, and Dr. Michał J. Michałowski for careful readings of the manuscript and providing valuable comments.

This scientific work uses data obtained from Inyarrimanha Ilgari Bundara/the Murchison Radio-astronomy Observatory. We acknowledge the Wajarri Yamaji People as the Traditional Owners and native title holders of the Observatory site. The Australian SKA Pathfinder is part of the Australia Telescope National Facility, [17] which is managed by CSIRO. Operation of ASKAP is funded by the Australian Government with support from the National Collaborative Research Infrastructure Strategy. ASKAP uses the resources of the Pawsey Supercomputing Centre. The establishment of ASKAP, the

[17] https://ror.org/05qajvd42

Murchison Radio-astronomy Observatory, and the Pawsey Supercomputing Centre are initiatives of the Australian Government, with support from the Government of Western Australia and the Science and Industry Endowment Fund. The POSSUM project [18] has been made possible through funding from the Australian Research Council, the Natural Sciences and Engineering Research Council of Canada, the Canada Research Chairs Program, and the Canada Foundation for Innovation. This research has made use of data obtained from the Chandra Data Archive provided by the Chandra X-ray Center (CXC).

Facilities: ASKAP, CXO.

Software: ASKAPsoft (J. Guzman et al. 2019), Astronomy-oriented Python packages: astropy (Astropy Collaboration et al. 2013, 2018, 2022), pyregion, General-purpose Python packages: matplotlib (J. D. Hunter 2007), numpy (T. Oliphant 2006).

ORCID iDs

Wenhui Jing https://orcid.org/0009-0004-4090-9304
Jennifer L. West https://orcid.org/0000-0001-7722-8458
Xiaohui Sun https://orcid.org/0000-0002-3464-5128
Wasim Raja https://orcid.org/0000-0002-6155-9962
Xianghua Li https://orcid.org/0000-0002-9399-8433
Lingxiao Dang https://orcid.org/0009-0006-1753-7623
Ping Zhou https://orcid.org/0000-0002-5683-822X
Miroslav D. Filipović https://orcid.org/0000-0002-4990-9288
Andrew M. Hopkins https://orcid.org/0000-0002-6097-2747
Roland Kothes https://orcid.org/0000-0001-5953-0100
Sanja Lazarević https://orcid.org/0000-0001-6109-8548
Denis Leahy https://orcid.org/0000-0002-4814-958X
Emil Lenc https://orcid.org/0000-0002-9994-1593
Yik Ki Ma https://orcid.org/0000-0003-0742-2006
Cameron L. Van Eck https://orcid.org/0000-0002-7641-9946

References

Arnaud, K. A. 1996, in ASP Conf. Ser. 101, Astronomical Data Analysis Software and Systems V, ed. G. H. Jacoby & J. Barnes (San Francisco, CA: ASP), 17
Asplund, M., Grevesse, N., Sauval, A. J., & Scott, P. 2009, ARA&A, 47, 481
Astropy Collaboration, Price-Whelan, A. M., Lim, P. L., et al. 2022, ApJ, 935, 167
Astropy Collaboration, Price-Whelan, A. M., Sipőcz, B. M., et al. 2018, AJ, 156, 123
Astropy Collaboration, Robitaille, T. P., Tollerud, E. J., et al. 2013, A&A, 558, A33
Ball, B. D., Kothes, R., Rosolowsky, E., et al. 2023, MNRAS, 524, 1396
Bamba, A., Shibata, S., Tanaka, S. J., et al. 2022, PASJ, 74, 1186
Beck, R., & Krause, M. 2005, AN, 326, 414
Berezhko, E. G., & Völk, H. J. 2004, A&A, 427, 525
Bhalerao, J., Park, S., Schenck, A., Post, S., & Hughes, J. P. 2019, ApJ, 872, 31
Bietenholz, M. F., & Bartel, N. 2008, MNRAS, 386, 1411
Bietenholz, M. F., Matheson, H., Safi-Harb, S., Brogan, C., & Bartel, N. 2011, MNRAS, 412, 1221
Blondin, J. M., Chevalier, R. A., & Frierson, D. M. 2001, ApJ, 563, 806
Bocchino, F., van der Swaluw, E., Chevalier, R., & Bandiera, R. 2005, A&A, 442, 539
Borkowski, K. J., Reynolds, S. P., & Roberts, M. S. E. 2016, ApJ, 819, 160
Brentjens, M. A., & de Bruyn, A. G. 2005, A&A, 441, 1217
Cassam-Chenaï, G., Decourchelle, A., Ballet, J., & Ellison, D. C. 2005, A&A, 443, 955
Cassam-Chenaï, G., Hughes, J. P., Reynoso, E. M., Badenes, C., & Moffett, D. 2008, ApJ, 680, 1180
Cigan, P., 2019 MultiColorFits: Colorize and Combine Multiple Fits Images for Visually Aesthetic Scientific Plots, Astrophysics Source Code Library, ascl:1909.002
Condon, J. J., Griffith, M. R., & Wright, A. E. 1993, AJ, 106, 1095
Doi, Y., Takita, S., Ootsubo, T., et al. 2015, PASJ, 67, 50
Dubner, G., & Giacani, E. 2015, A&ARv, 23, 3
Duncan, A. R., Stewart, R. T., Haynes, R. F., & Jones, K. L. 1995, MNRAS, 277, 36
Ellison, D. C., Decourchelle, A., & Ballet, J. 2005, A&A, 429, 569
Enokiya, R., Sano, H., Filipović, M. D., et al. 2023, PASJ, 75, 970
Ferrand, G., & Safi-Harb, S. 2012, AdSpR, 49, 1313
Filipović, M. D., Dai, S., Arbutina, B., et al. 2023, AJ, 166, 149
Fruscione, A., McDowell, J. C., Allen, G. E., et al. 2006, Proc. SPIE, 6270, 62701V
Gaensler, B. M., Landecker, T. L., Taylor, A. R. & POSSUM Collaboration 2010, BAAS, 42, 515
Gaensler, B. M., & Slane, P. O. 2006, ARA&A, 44, 17
Gaensler, B. M., & Wallace, B. J. 2003, ApJ, 594, 326
Griffith, M. R., & Wright, A. E. 1993, AJ, 105, 1666
Guest, B. T., Safi-Harb, S., & Tang, X. 2019, MNRAS, 482, 1031
Gaensler, B. M., et al. 2024, PASA, submitted
Guzman, J., Whiting, M., Voronkov, M., et al., 2019 ASKAPsoft: ASKAP science data processor software, Astrophysics Source Code Library, ascl:1912.003
Haverkorn, M., Brown, J. C., Gaensler, B. M., & McClure-Griffiths, N. M. 2008, ApJ, 680, 362
Heald, G. 2009, in IAU Symp. 259, Cosmic Magnetic Fields: From Planets, to Stars and Galaxies, ed. K. G. Strassmeier, A. G. Kosovichev, & J. E. Beckman, 591
HI4PI Collaboration, Ben Bekhti, N., Flöer, L., et al. 2016, A&A, 594, A116
Hotan, A. W., Bunton, J. D., Chippendale, A. P., et al. 2021, PASA, 38, e009
Hunter, J. D. 2007, CSE, 9, 90
Katsuda, S. 2017, in Handbook of Supernovae, ed. A. W. Alsabti & P. Murdin (Berlin: Springer), 63
Kolb, C., Blondin, J., Slane, P., & Temim, T. 2017, ApJ, 844, 1
Kothes, R. 2017, in Handbook of Supernovae, ed. A. W. Alsabti & P. Murdin (Berlin: Springer), 97
Kothes, R., Landecker, T. L., Reich, W., Safi-Harb, S., & Arzoumanian, Z. 2008, ApJ, 687, 516
Kothes, R., Reich, W., Safi-Harb, S., et al. 2020, MNRAS, 496, 723
Kothes, R., Reich, W., & Uyanıker, B. 2006, ApJ, 638, 225
Lazarević, S., Filipović, M. D., Koribalski, B. S., et al. 2024, RNAAS, 8, 107
Lazendic, J. S., Slane, P. O., Gaensler, B. M., et al. 2004, ApJ, 602, 271
Ma, Y. K., Ng, C. Y., Bucciantini, N., et al. 2016, ApJ, 820, 100
Manchester, R. N., Hobbs, G. B., Teoh, A., & Hobbs, M. 2005, AJ, 129, 1993
Martin, J., Torres, D. F., Cillis, A., & de Oña Wilhelmi, E. 2014, MNRAS, 443, 138
Murphy, T., Mauch, T., Green, A., et al. 2007, MNRAS, 382, 382
Norris, R. P., Hopkins, A. M., Afonso, J., et al. 2011, PASA, 28, 215
Norris, R. P., Marvil, J., Collier, J. D., et al. 2021, PASA, 38, e046
Oliphant, T. 2006, NumPy: A guide to NumPy (USA: Trelgol Publishing) http://www.numpy.org/
Olmi, B., & Bucciantini, N. 2023, PASA, 40, e042
Pacholczyk, A. G. 1970, Series of Books in Astronomy and Astrophysics (San Francisco, CA: Freeman),
Pejcha, O., & Prieto, J. L. 2015, ApJ, 806, 225
Porth, O., Vorster, M. J., Lyutikov, M., & Engelbrecht, N. E. 2016, MNRAS, 460, 4135
Purcell, C., Van Eck, C. L., West, J., Sun, X. H., & Gaensler, B. M., 2020 RM-Tools: Rotation measure (RM) synthesis and Stokes QU-fitting, Astrophysics Source Code Library, ascl:2005.003
Ranasinghe, S., & Leahy, D. 2023, ApJS, 265, 53
Rau, U. 2010, Phd thesis, New Mexico Institute of Mining and Technology
Renaud, M., Marandon, V., Gotthelf, E. V., et al. 2010, ApJ, 716, 663
Reynolds, S. P., & Borkowski, K. J. 2019, ApJ, 887, 233
Reynolds, S. P., & Borkowski, K. J. 2024, ApJ, 962, 179
Reynolds, S. P., Borkowski, K. J., Green, D. A., et al. 2008, ApJL, 680, L41
Reynolds, S. P., & Chevalier, R. A. 1981, ApJ, 245, 912
Reynolds, S. P., Gaensler, B. M., & Bocchino, F. 2012, SSRv, 166, 231
Rho, J., Dyer, K. K., Borkowski, K. J., & Reynolds, S. P. 2002, ApJ, 581, 1116
Robbins, W. 2014, Phd thesis, Univ. Sydney
Sato, T., Katsuda, S., Morii, M., et al. 2018, ApJ, 853, 46
Slane, P., Hughes, J. P., Temim, T., et al. 2012, ApJ, 749, 131
Smeaton, Z. J., Filipović, M. D., Lazarević, S., et al. 2024, MNRAS, 534, 2918
Sokoloff, D. D., Bykov, A. A., Shukurov, A., et al. 1998, MNRAS, 299, 189
Tanaka, S. J., & Takahara, F. 2013, MNRAS, 429, 2945
Tang, X., & Chevalier, R. A. 2012, ApJ, 752, 83
Tomsick, J. A., Chaty, S., Rodriguez, J., Walter, R., & Kaaret, P. 2009, ApJ, 701, 811

[18] https://possum-survey.org

van der Swaluw, E. 2003, A&A, 404, 939
van der Swaluw, E., Downes, T. P., & Keegan, R. 2004, A&A, 420, 937
van der Swaluw, E., & Wu, Y. 2001, ApJL, 555, L49
Vanderwoude, S., West, J. L., Gaensler, B. M., et al. 2024, AJ, 167, 226
Villagran, M. A., Gómez, D. O., Velázquez, P. F., et al. 2024, MNRAS, 527, 1601
Vink, J. 2020, Physics and Evolution of Supernova Remnants, Astronomy and Astrophysics Library (Berlin: Springer),
Wright, E. L., Eisenhardt, P. R. M., Mainzer, A. K., et al. 2010, AJ, 140, 1868
Yao, J. M., Manchester, R. N., & Wang, N. 2017, ApJ, 835, 29
Zhu, B.-T., Zhang, L., & Fang, J. 2018, A&A, 609, A110
Zirakashvili, V. N., & Aharonian, F. A. 2010, ApJ, 708, 965